Improved charge separation and surface activation *via* boron-doped layered polyhedron SrTiO₃ for co-catalyst free photocatalytic CO₂ conversion

Jingjing Shan[a], Fazal Raziq[a], Muhammad Humayun[a], Wei Zhou[a], Yang Qu[a,*], Guofeng Wang[a,*], Yadong Li[b]

[a] *Key Laboratory of Functional Inorganic Materials Chemistry (Heilongjiang University), Ministry of Education, School of Chemistry and Materials Science, International Joint Research Center for Catalytic Technology, Harbin 150080, China*
[b] *Department of Chemistry, Tsinghua University, Beijing, 100084, China*

ARTICLE INFO

ABSTRACT

For efficient photocatalytic CO₂ conversion to solar fuel, it is highly desired to enhance the solar-light absorption, photogenerated charge separation and surface active/catalytic performance of semiconductor photocatalysts. Herein, we have successfully prepared boron-doped layered polyhedron SrTiO₃ (STO) by solid-state method using specific TiB₂ precursor as boron and titanium resource. The prepared polyhedron STO is single-crystal structure with average diameter of ∼500 nm and boron-doped STO exhibits overlapped-layer structure. The boron doping amount could be controlled using TiB₂. It is shown that the amount optimized boron-doped layered polyhedron STO sample Exhibit 3-times enhanced co-catalyst free photocatalytic activity for CO₂ conversion, compared to the bare STO nanoparticles. Notably, the improved photocatalytic performance could be attributed to the enhanced charge separation as confirmed by means of fluorescence emission spectra related to produced •OH radicals, surface photovoltage responses and photoelectrochemical measurements; and the enhanced CO₂ surface adsorption and catalytic performance of boron-doped SrTiO₃ as verified by CO₂-TPD and electrochemical CO₂ reduction experiments. This work implies that boron-doped layered polyhedron SrTiO₃ would display promising applications in the photocatalytic field of CO₂ conversion to solar fuels.

© 2017 Elsevier B.V. All rights reserved.

1. Introduction

With the rapid development of industrialization, electrification and urbanization, the generous use of non-renewable fossil fuels have caused a series of hazardous environmental problems. Meanwhile, the intensity of the fossil energy shortage is continuously increasing. Hence, it is highly desirable to develop green and sustainable technologies for clean energy production and environmental remediation. As widely accepted, CO₂ is one of the reasons for global warming because of the excessive emission from industry. [1,2] However, as a common small C1 organic molecule, it is also used as a major ingredient for synthesizing medicine, plastics, dyes and fuels. As a result, the rational utilization of CO₂ as natural resources is extremely important for both the energy and environmental issues. [3] In the past few years, photocatalytic

CO₂ conversion over semiconductor photocatalysts under solar-irradiation has been regarded to be a potential candidate to reduce CO₂ emission. [4–6] Photocatalytic CO₂ reduction have so far displayed much exciting prospect, but the activity is still very low because of the complex reaction which undergoes many thermodynamic and kinetic steps and some of them are even unclear up to now. [7] Current studies suggested that the electronic structure, surface state and charge separation of semiconductor photocatalysts are much important for efficient photocatalysis.

Among the widely investigated semiconductors, perovskite-type metal oxides are regarded as promising photocatalysts owing to their outstanding optical properties, photo-stability and low cost. [8–10] As a typical perovskite oxide, SrTiO₃ (Eg = 3.2 eV) has attracted much attention due to its more negative conduction band position, photochemical stability and high photocatalytic efficiency for pollutants degradation, water splitting and CO₂ reduction. [11–13] Hemminger and his co-workers reported the photosynthetic reduction of carbon dioxide in water vapor to produce methane over the crystalline surface of STO in the absence of any

electrolyte and external potential. [14] However, the photocatalytic applications of STO are still unsatisfactory due to the limited light absorption (only UV–light, ca. 5% of the solar-spectrum), the fast recombination of photogenerated charges and the weak surface absorption. Therefore, it is highly desirable to improve the light absorption, charge separation and surface CO_2 absorption of STO so as to promote its photocatalytic activity for CO_2 reduction. Generally speaking, the O2p and Ti3d orbital respectively constitute the valence band and conduction band of STO. It has been previously demonstrated that doping metal or non-metal elements could introduce new energy levels that results in the narrowed band gap. [15,16] A series of transition metal elements have been tried to tune its electronic bandgap for harvesting visible light. [17–19] Unfortunately, doping these elements results in the impurity phases or fast recombination of photogenerated charge carriers, which is still a challenge for the scientific researchers.

Replacing partial O in the metal oxides by anion is a convenient strategy to raise the valence band maxima. Anionic non-metal doping, such as boron, carbon, nitrogen, sulfur and fluorine atoms, have been widely investigated and regarded to be an effective strategy to enhance the light absorption and charge separation of wide band gap semiconductors. [20–22] Boron (B) is an important non-metal element for doping, as demonstrated by G. Liu's group that B doped TiO_2 material possesses outstanding photocatalytic activity for hydrogen production and organic pollutant degradation. [23] Some previous works have shown the advances of B doped STO in photocatalysis. Y. Jia's group has found that B may be the best candidate for doping in STO, based on the first-principles density-functional calculation. [24] H. Yu et al. have demonstrated that B doping could activate visible-light absorption of STO. [25] Besides, the non-metal doping is an efficient strategy to turn the internal electric field which is induced by the polarization of the non-uniform charge distribution between different constituent layers and enables separation of electrons and holes immediately after their generation. [26] The B doping could result in the upward drift of Fermi level and flat band. This changing will heighten the surface potential barrier and narrow down the space-charge region that the photogenerated electron-hole pairs are effectively separated with the force of the strong internal electric field. [27] Hence, B doping is a suitable choice to improve the light absorption and charge separation of STO.

Before catalyzing CO_2 to solar fuels, the activation of it is regarded as the key step, however, the absorption of CO_2 is the precondition for activation. [28] The chemisorption state CO_2, mainly carbonate and/or CO_2 anion, has a bent O—C—O bond angle and a decreased LUMO, which is beneficial to the charge transfer from photo-excited semiconductors to the surface adsorbed CO_2 molecules. [29] Therefore, surface absorption chemistry plays significant role to CO_2 activation. It is rather effective to increase the surface fixation of CO_2 on photocatalysts for a relatively high photocatalytic activity. The photocatalytic CO_2 reduction activity of STO could be enhanced by doping B, because of the vacant atomic orbitals of B element. [30] The B on the surface of STO acts as active sites for activation of the adsorbed CO_2 and the activated CO_2 molecules are reduced by the photogenerated electrons of STO. Hence, it is much meaningful to prepare B doped STO for photocatalytic CO_2 reduction *via* effective synthetic method.

Solid state method is well applied in preparing perovskite materials. [31] Materials with single crystal or other morphologies are usually found through solid state method. For preparing B doped STO by solid state method, the resource of B is also significant because it is relative to the surface and crystallinity of the material. Titanium boride (TiB_2), as a boron source is suitable for B doped STO because it could provide both Ti and B simultaneously. [32] In addition, few works have shown that B could diffuse from bulk to surface during the synthesis of B-doped TiO_2 *via* solid state method.

[23,32] This phenomenon brings new information that the surface doping of B on STO could be controlled using TiB_2 as a boron source.

Based on the above consideration, we report boron-doped layered polyhedron STO which is prepared through solid-state method using TiB_2 as boron and titanium resource. The as-prepared material is single crystal with assembled layered-structure and high crystallinity as confirmed by means of XRD, SEM and TEM analysis. As expected, the solar light absorption of STO is extended after doping B, owing to the newly formed energy levels near the VB top. Interestingly, the surface adsorption for CO_2 and the charge separation of boron-doped layered STO polyhedron are also promoted. As a result, the material exhibits excellent co-catalyst free photocatalytic activity for CO_2 reduction.

2. Experimental section

2.1. Material synthesis

Strontium carbonate ($SrCO_3$; AR) was obtained from sinopharm chemical reagent and $Ti(OC_4H_9)_4$ was purchased from Kermel chemical reagent. Titanium boride (TiB_2; AR) was supplied by Xiya reagent. All the chemicals were of analytical grade and used as-received without further purification. For the synthesis of $SrTiO_3$ nanoparticles, [33] in a typical experiment, 0.74 g of $SrCO_3$ and 1.7 ml of $Ti(OC_4H_9)_4$ were dissolved in 10 ml absolute ethanol. At the same time, 5 drops of concentrated hydrochloric acid were added to it to prevent the hydrolysis. Then the solution was mechanically milled with a planetary ball milling apparatus at 150 runs min^{-1} for 3 h. Subsequently, the obtained product was collected by constant temperature heating blender, washed with ethanol, and dried in air at 80 °C. Finally the dry white powder was annealed in air at 1100 °C (temp ramp 2 °C min^{-1}) for 2 h to obtain the phase purity $SrTiO_3$ nanoparticles and denoted as STO.

For the synthesis of B-doped STO sample, in a typical process, 0.74 g $SrCO_3$, 0.02 g TiB_2 and 1.66 ml $Ti(OC_4H_9)_4$ were dissolved in 10 ml of absolute ethanol. At the same time, 5 drops of concentrated hydrochloric acid were added to it to prevent the hydrolysis. The rest of the procedure was the same as above. Thus, the theoretical 10 mol% boron doping of STO sample was obtained. For comparison, different mole percentage (*i.e.* 10, 20 and 30%) of B-doped STO samples were prepared under identical conditions and denoted as B-STO-X (X = 10, 20 and 30).

2.2. Characterization

The XRD patterns of the material were characterized with the help of a Bruker D8 Advance X-ray diffractometer equipped with a graphite monochromatized Cu Kα radiation (γ = 1.541874 Å). The size and morphology of the final products were investigated by scanning electron microscopy (SEM, Hitachi, S-4800) and Transmission electron microscopy (TEM, JEOL, JEM-2100). UV–vis absorption spectra were obtained with the help of a UV–vis spectrophotometer (Shimadzu UV-2550, Tokyo, Japan). The specific surface area was determined according to the Brunauer-Emmett-Teller (BET) method using a Tristar II 3020 surface area and porosity analyzer (micromeritics). X-ray Photoelectron Spectroscopy (XPS) analysis were carried out using a Kratos-AXIS ULTRA DLD apparatus with Al (Mono) X-ray source, and the binding energies of the samples were calibrated with respect to the signal for adventitious carbon (binding energy = 284.6 eV).

2.3. Photoelectrochemical measurements

For the synthesis of thin film electrodes, conductive fluorine-doped tin oxide (FTO)-coated glasses were used as substrates. Prior to use, the FTO glasses were washed with deionized water under
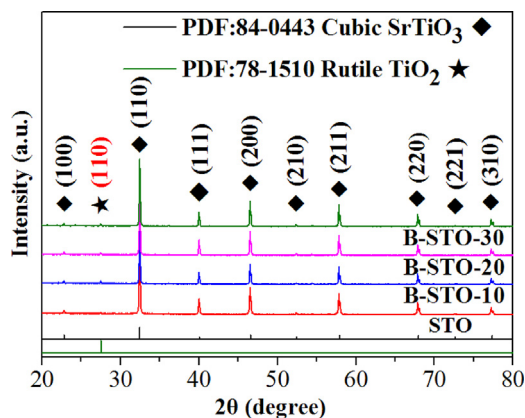
Fig. 1. XRD patterns of SrTiO₃ prepared with different B doping: STO, B-STO-10, B-STO-20, and B-STO-30.

sonication for 30 min and then washed with ethanol followed by deionized water and finally annealed at 450 °C for 30 min. The corresponding pastes for the samples were prepared as follows: 0.1 g of the resulting sample powder was dispersed in 1 ml of isopropyl alcohol under vigorous stirring, and then 0.05 g of Macrogol-2000 was added to the mixture, followed by an ultrasonic treatment for 10 min and then kept under vigorous stirring for 30 min. Finally, 0.15 ml of acetyl acetone was added to it, and the mixture was kept under continuous stirring for 7 days. The films were prepared by a doctor blade method, and Scotch tape was used as the spacer. After dried naturally, the film was annealed at 450 °C for 30 min and then cooled to room temperature. Finally, the film was cut into $1.0 \times 1.5 \, cm^2$ pieces. The working geometric surface area of the samples film was 1 cm × 1 cm.

Photoelectrochemical (PEC) experiments were performed in a quartz cell using a 500 W xenon light with a stabilized current power supply as the illumination source and 1 M NaOH solution was used a as an electrolyte. The as-prepared films were used as working electrodes illuminated from the FTO glass side, whose illu-

mination area was about $1 \times 1 \, cm^2$. A platinum plate (99.9%) was used as the counter electrode, and a saturated KCl Ag/AgCl electrode (SSE) was used as the reference electrode. All the potentials in this work were referred to SSE at 298 K, and applied potentials were controlled by a commercial computer-controlled potentiostat (AUTOLAB PG STAT 101). High-purity N_2 gas was employed to bubble through the electrolyte before the experiments. For comparison, the related current was also measured in the dark. TPD studies were performed using a CHEMBET-3000 (Quantachrome, U.S.A.) instrument in the temperature range of 313–1073 K.

2.4. Evaluation of photocatalytic activities for CO2 reduction

In the photocatalytic reduction of CO_2, for each experiment, 0.2 g of powder sample was dispersed in 2 ml of water contained in a 100 ml volume of cylindrical steel reactor with area 3.5 cm². A 300 W Xenon arc lamp was used as the light source for photocatalytic reaction. High purity CO_2 gas was passed from the water and followed into the reaction setup to reach the ambient pressure. The used photocatalyst was allowed to equilibrate in the CO_2/H_2O system for 1 h. During the irradiation, about 0.5 ml of the produced gas was taken from the reaction cell at given time interval for the concentration analysis of main products such as CO and CH_4 using a gas chromatograph (GC-2014 with TCD detector; Shimadzu Corp, Japan and GC-7900, FID).

2.5. Hydroxyl radical measurement

To detect the amount of hydroxyl radical produced, coumarin fluorescent method was used. In coumarin fluorescent method, 0.02 g powder was dispersed in 50 ml coumarin aqueous solution (0.001 M) in a beaker. Prior to irradiation, the reactor was magnetically stirred for 10 min to attain an adsorption-desorption equilibrium. After irradiation for 1 h with a 150 W GYZ220 high-pressure Xenon lamp (made in China), the sample was centrifuged, and then a certain volume of solution was transferred into a Pyrex glass cell for the fluorescence measure-
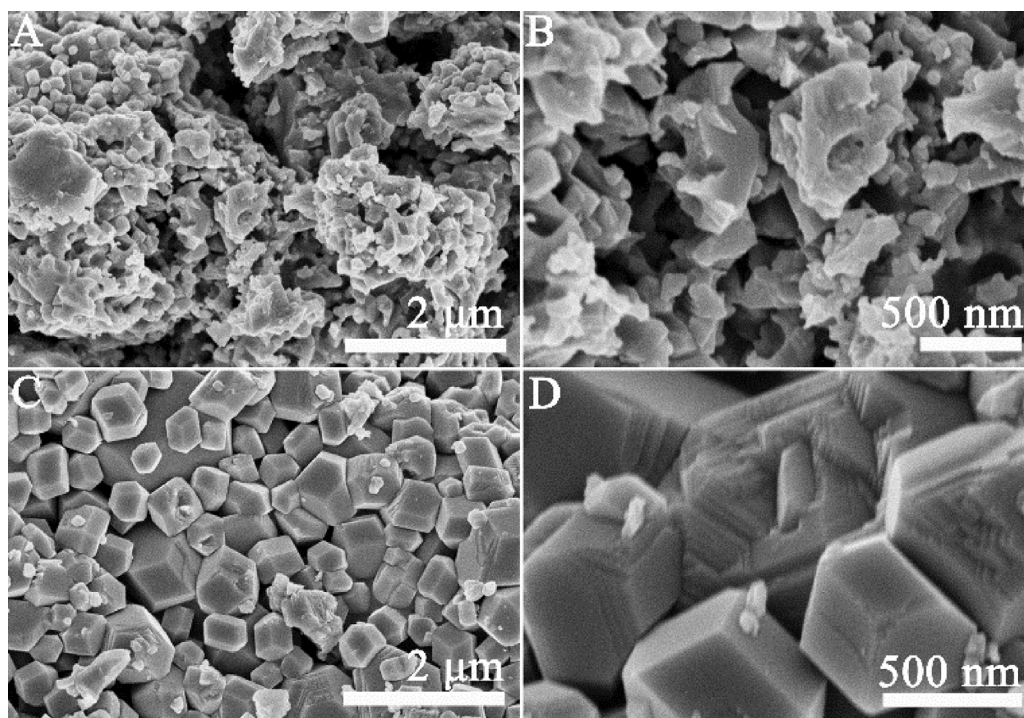

Fig. 2. SEM images (A, B) of STO and (C, D) of B-STO-20 samples.

ment of 7-hydroxycoumarinat 332 nm excitation wavelength with an emission wavelength at 456 nm through a spectrofluorometer (Perkin-Elmer LS55).

3. Results and discussion

The phase purity of the as-prepared STO and B-STO-X (X = 10, 20 and 30) samples were studied by powder X-ray diffractometer (XRD). From Fig. 1, it is clear that the corresponding peaks at 2θ = 22.8, 32.5, 40, 46.6, 52.4, 57.9, 69.9 and 77.4° are ascribed to the cubic phase of perovskite-type $SrTiO_3$ (JCPDS 84-0443). The strong peaks imply high crystallinity of the product. Despite the solid state method, nanomaterials with high crystallinity could be prepared, and the impurity is often introduced as well. It is found that rutile TiO_2 phase (JCPDS 78-1510) appeared at 2θ = 27.5° (the main diffraction peak of rutile) for all samples due to the associated impurities produced under high temperature treatment. [34] In addition, the intensity of rutile phase TiO_2 in the XRD patterns gradually become strong with the increase of TiB_2 amount, as shown in Fig. S1.

The morphology of photocatalysts is significant because it is relative to the light absorption and charge separation. To investigate the morphology of STO and B-STO-20 samples, SEM images were taken as shown in Fig. 2. It is clear that the STO particles exhibit irregular shapes with nanometric sizes and the average diameters ranges from 500 to 1500 nm (Fig. 2A, B). However, after doping B, the irregular particles have been changed to uniform ones as shown in Fig. S2 and Fig. 2C. Among them, B-STO-20 sample possesses the optimal morphology and is consistent with polyhedron hexagonal prisms structure. The particles size distribution is from 500 to 800 nm. In addition, the layered structure of polyhedron STO particles could be seen from the high resolution SEM image of the broken ones as shown in Fig. 2d. It is inferred that the polyhedron STO is assembled by hexagonal nanosheets.

It has been previously reported that TiB_2 play a bifunctional role of B-doping and morphology turning. [32] When TiB_2 is annealed at high temperature, B would diffuse from bulk to surface, and replace O of the TiO_6 lattice, then locate on the surface of STO and favors the assemble of these nanosheets to polyhedron. To verify this, FT-IR spectra of STO and B-STO-X samples were measured and shown in Fig. S3. Compared with the FT-IR spectrum of STO, two extra bands at 1100 and 1370 cm^{-1} are observed in all B-STO-X. The band at ca. 1370 cm^{-1} can be ascribed to the presence of tricoordinated interstitial B, which tends to interact with ambient O

atoms and exhibits a chemical environment similar to that of normal Ti—O—B. [35] The peak at 1100 cm^{-1} can be attributed to the stretching vibrations of the B—O bonds. The B—O bond formed as a result of interaction between interstitial B and its neighbor O. In brief, the afore-discussed FT-IR results reveal that some B species in the B-doped STO are present as interstitial B, nevertheless, the existence of O-substituted B may not be ruled out.

To further investigate the layered structure of the polyhedron STO, TEM and HRTEM images were taken. The TEM image of B-STO-20 gives the evidence of the layered STO accumulated into polyhedron, proven by the hexagonal nanosheet-like fragment could be observed from Fig. 3A of which may come from the edge of polyhedron just like the selected area in Fig. 2D. The TEM images of STO, B-STO-10 and B-STO-30 samples are shown in Fig. S4, which are in accordance with the SEM images. The HRTEM image of B-STO-20 sample (Fig. 3B) shows that the lattice fringes with d-spacing 0.18 nm correspond to the (110) plane of the cubic phase STO. The diffraction spots from selected area electron diffraction (SAED) patterns (as inset in Fig. 3B) clearly demonstrate that the B-STO-20 sample is single crystalline. The single crystal structure usually has very few defects that favor charge transfer and separation. From the structural characterization of the samples, it can be learned that the morphology of the as-prepared nanoparticles changed to hexagonal polyhedron with layered structure when TiB_2 is utilized to prepare B doped STO. Moreover, the as-prepared B-doped STO is monocrystal which is similar to other materials obtained by solid state method. For perovskite photocatalysts, the morphology and crystallinity is much important for photoactivities. The B-doped STO is believed to be a promising material for photocatalytic CO_2 reduction.

The composition and elemental chemical states of STO and B-STO-X samples were investigated by X-ray photoelectron spectroscopy (XPS). The general XPS survey spectra in Fig. S5, clearly indicates the existence of Ti, Sr and O elements in all the samples as well as B in the B-doped STO. In order to clarify the chemical environment of different elements, high resolution XPS spectra are shown in Fig. 4. Fig. 4A clearly demonstrates that the binding energy at 132.74 eV correspond to the Sr 3d which is in accordance with the previous works about perovskite STO, and the binding energy at 134.47 eV can be attributed to Sr-O complexes. [36] From high-resolution spectrum of Ti 2p (Fig. 4B), it is obvious that binding energy of B-STO sample is shifted toward lower energy side as compared to that of STO. It is supposed that the blue shift in the binding energy of Ti 2p is induced by the B-doping which can reduce the
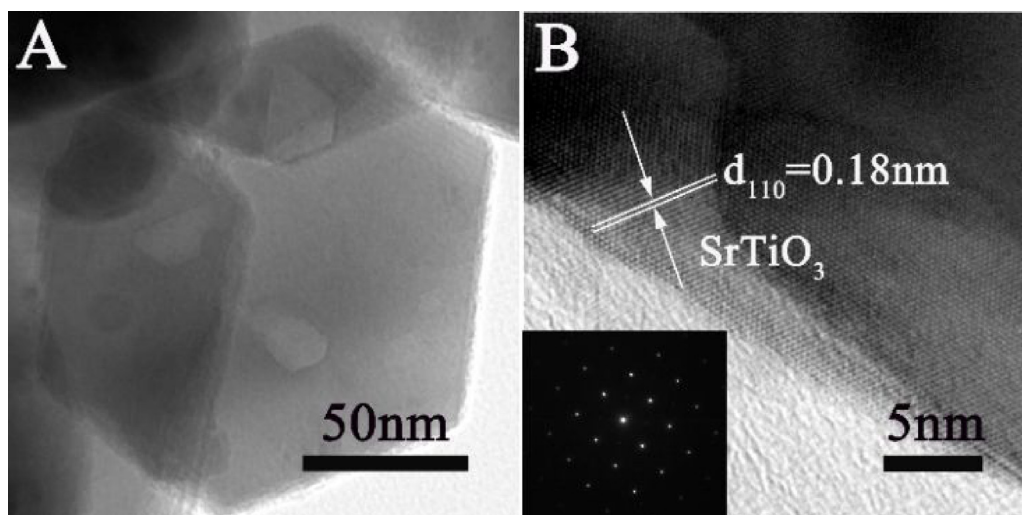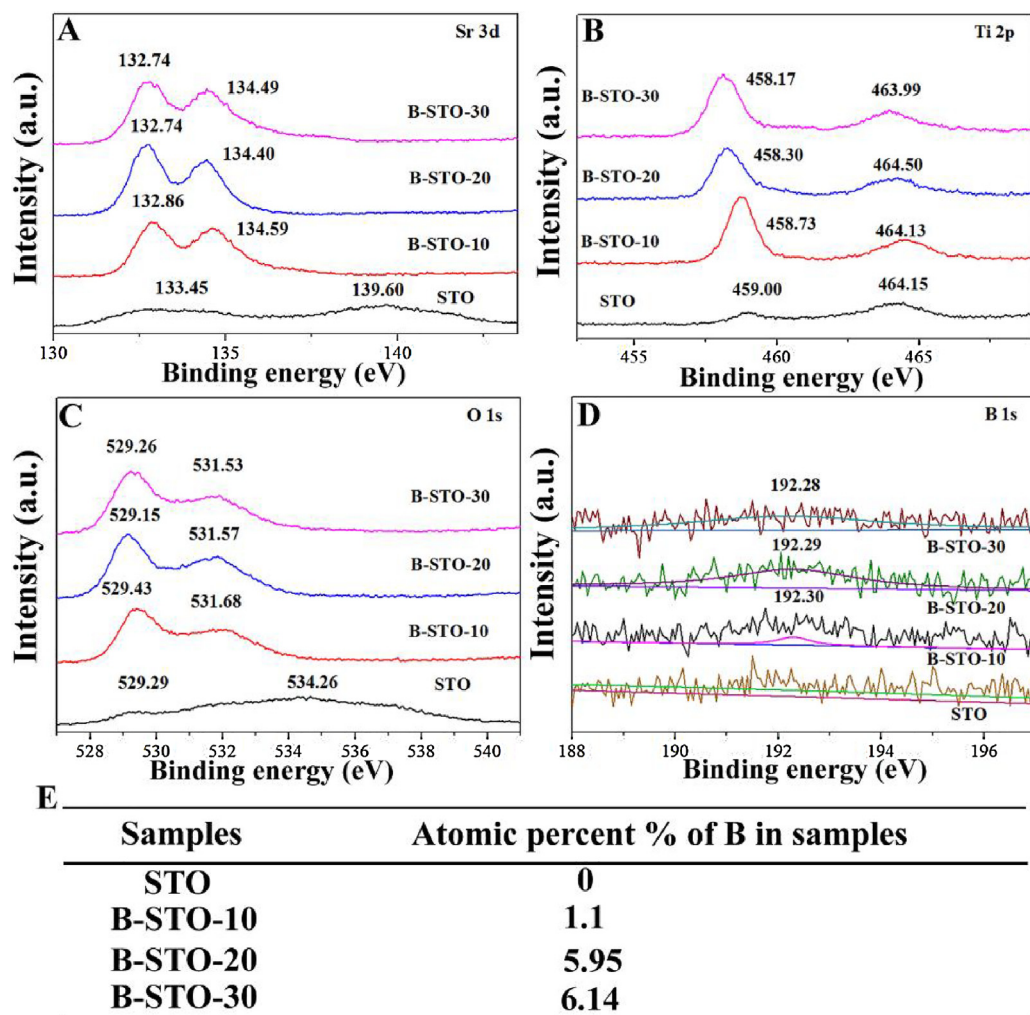

Fig. 3. TEM and HRTEM images (A, B) of B-STO-20 and the inset of B shows selected area electron diffraction (SAED) patterns.
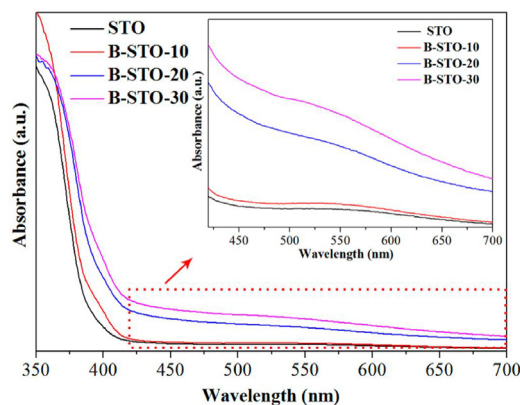
Fig. 4. XPS spectra of Ti 2p, O 1s, Sr 3d, B 1s (A–D), and (E) the relative B atomic percent given in the table for STO, B-STO-10, B-STO-20, and B-STO-30 samples.

Ti^{4+} to Ti^{3+} state. The XPS spectra of O 1s (Fig. 4C), show two small peaks, the peak centered at 529.56 eV is attributed to lattice oxygen of STO, while the other centered at 531.78 eV is related to the surface adsorbed oxygen, resulting from the carbonates and hydroxyl oxides.

As for B-STO samples, it is clear that the binding energy of O 1s is slightly shifted toward low energy side compared to the STO, suggesting that B is successfully incorporated in the crystal lattice of STO and substituted O atoms. As expected, the B 1 s peak at ∼192 eV (Fig. 4D) is attributed to the B—O bonds in the B-STO-10, B-STO-20 and B-STO-30 samples, and consistent with the FT-IR results. [37] These results suggest that B-doping has a great influence on the O sites as compared to the Ti sites, which is considered the evidence of Sr site substitution. Moreover, the real atomic percentage of B element in the B-doped SrTiO$_3$ samples is confirmed by XPS as well. As shown in Fig. 4E, the atomic percent of B in B-STO-10, B-STO-20 and B-STO-30 are 1.1, 5.9 and 6.1%, respectively. It can be learned from XPS and the other structural characterization that different contents B-doped polyhedron layered STO perovskite are prepared. However, it is shown that the amount of B doping could not be accurately controlled through the TiB$_2$ based solid-state method.

Fig. 5 shows the UV–vis absorption spectra of STO and B-STO-X samples. Compared to the STO, the B-doped samples display enhanced light absorption in visible-light region, implying the surface doping of boron. This surface doping may result from the diffusion of B from bulk to the surface after annealing, as reported

previously. [23] Interestingly, after B-doping the B-STO samples exhibit extended visible-light absorption from 420 to 700 nm (inset of Fig. 5). This enhancement in the light absorption is believed to have positive effect on the photocatalytic activities of the samples. For a crystalline semiconductor, the optical absorption near the band edge follows the equation $ah\nu = A(h\nu - E_g)^{n/2}$, where a, ν, E_g and A are the absorption coefficient, the light frequency, the bandgap and a constant, respectively. Among them, n decides the character-

Fig. 5. UV–vis absorption spectra of the STO and B-STO-X samples, the inset shows the local amplification in the range of 420–700 nm.
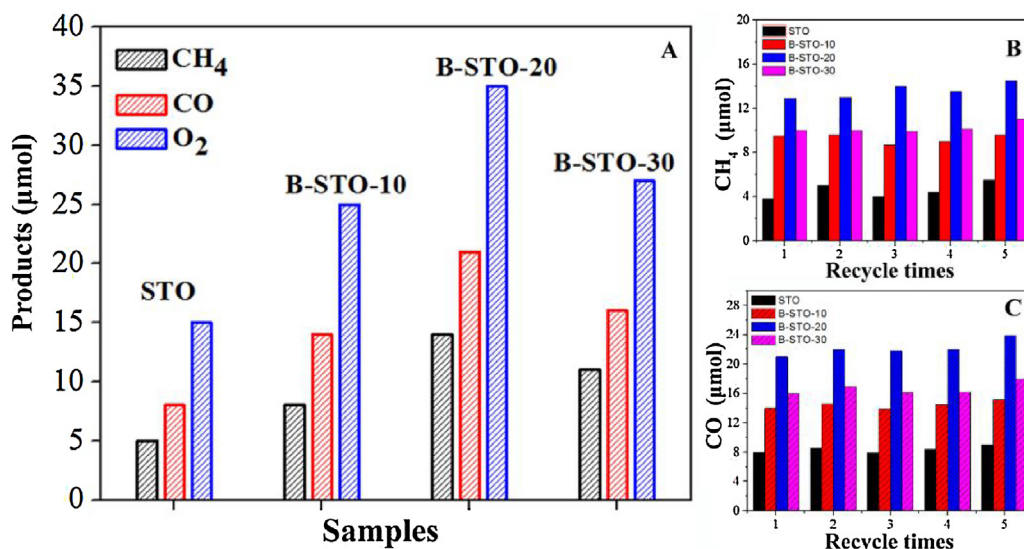
Fig. 6. The production rates of CH_4 during the photocatalytic CO_2 reduction with H_2O on STO, B-STO-10, B-STO-20, and B-STO-30.

istics of the transition in a semiconductor. [8] The bandgaps of STO, B-STO-10, B-STO-20, and B-STO-30 are calculated to be about 3.19, 3.18, 3.07 and 3.06 eV from the onset of the absorption edge (Fig. S6). The band gap narrowing of B-STO-20 and B-STO-30 samples may result from the increase in amount of rutile TiO_2 impurities which is in good agreement with the XRD results.

Thermodynamically, the conduction band of STO is negative enough to reduce CO_2 into CH_4, CO and so on. The co-catalyst free photoactivities of the as-prepared samples for CO_2 reduction are shown in Fig. 6A. Compared with the STO, the co-catalyst free photocatalytic activities of B-doped samples for CO_2 conversion to CO and CH_4 are remarkably enhanced. The production rate of CO is 8, 14, 21 and 16 $\mu mol\,h^{-1}\,g^{-1}$ and the yield of CH_4 is up to 5, 8, 14, and 11 $\mu mol\,h^{-1}\,g^{-1}$ for STO, B-STO-10, B-STO-20 and B-STO-30, respectively. Remarkably, O_2 as the oxydic product of water is found to 15, 25, 35 and 27 $\mu mol\,h^{-1}\,g^{-1}$ for STO, B-STO-10, B-STO-20 and B-STO-30, respectively. That means, according to the conservation of positive (for producing O_2 with 4 holes) and negative electron (for producing CO with 2 electrons and CH_4 with 8 electrons), some other products like methanol or formaldehyde may exist in the system. [38,39] Further, the organic products of methanol and formaldehyde are qualitatively detected by GC–MS, as shown in Fig. S7, supporting the above assumption. Interestingly, the amount optimized B-STO-20 sample exhibits nearly three times enhanced activity as compared to that of STO. In addition, the apparent quantum efficiency (AQE) is 1.34% for B-STO-20, along with 0.53% for STO at 365 nm. However, there is no AQE for STO while 0.53% for B-STO-20 at 420 nm, suggesting that a proper B doping can improve the visible light absorption. It is worth noting that the amount of CO and CH_4 produced over B-doped STO without any co-catalyst in this work is superior as compared to some related works, as shown in Table S1. These results indicate that B-doping has a positive effect on the photocatalytic activity of STO for CO_2 reduction. Once CO_2 was replaced with N_2, the evolution of CO and CH_4 was also not observed, thus the suspected CO and CH_4 from surroundings and surface adsorption of photocatalysts are excluded. To further confirm the source of the produced CH_4, we carried out an isotopic experiment using [13]CO_2 under the identical photocatalytic reaction conditions. The photocatalytic evolution of CH_4 was analyzed by gas chromatography mass (GC–MS), of which the peak m/z = 17 is assigned to [13]CH_4 and the fragment ion of [13]CH_4 is seen as well as shown in Fig. S8. In addition, the stability of STO and B-STO-X samples are investigated by five times run recycles, each
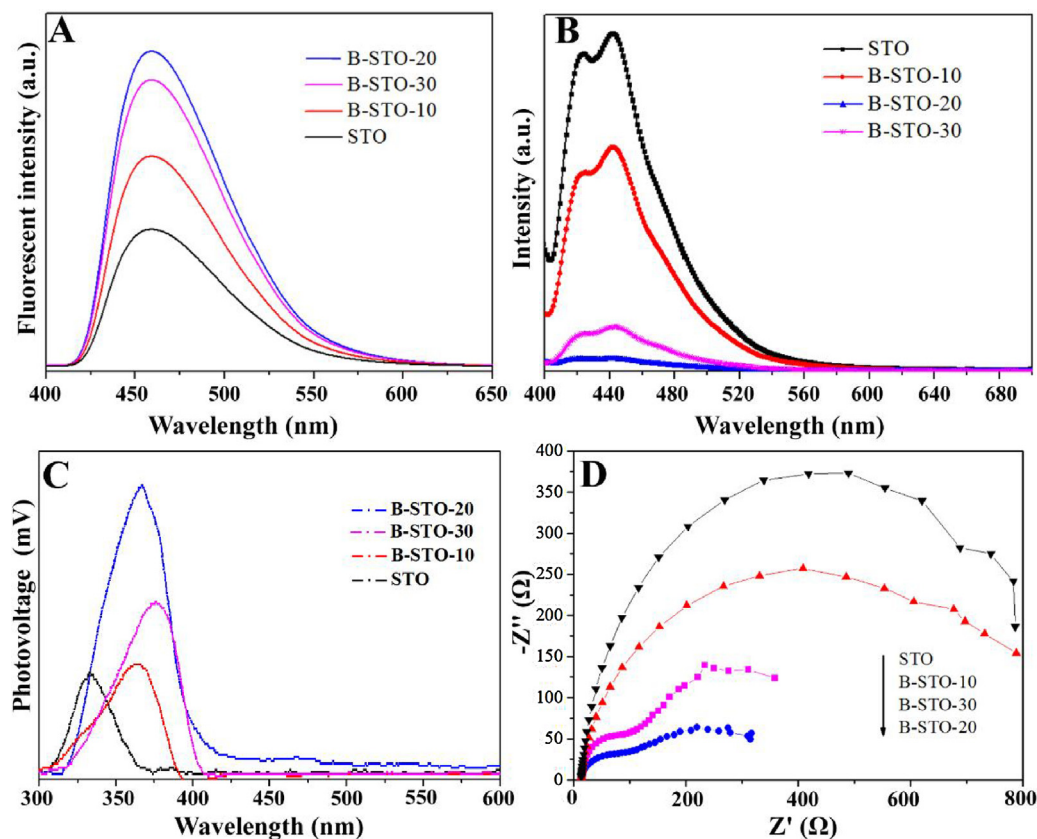
time washing the samples with water and absolute ethanol and then drying at 100 °C. It can be seen that after five successive recycles, the B-doped samples exhibit good stability for photocatalytic CO_2 reduction as shown in Fig. 6B and C.

There are many effects that cause the enhanced activity of B-doped STO, including surface area, charge transfer and separation and so on. In order to verify the surface area, N_2 absorption and desorption isotherms of STO and B-STO-X samples were measured as shown in Fig. S9. The surface area of the resultant STO photocatalyst obtained *via* solid state synthesis is very small because of the high temperature treatment. However, the surface area is remarkably increased after B-doping even if the B content is 30%, which may be attributed to the its broken morphology. This is in accordance with the SEM images that the morphology changed after B-doping. The nearly three times enhanced surface area may result in the improved CO_2 adsorption over the photocatalyst surface, which favors the surface catalyzing reactions.

Charge separation is the main affecting factor for the activity of photocatalysts. [40] The produced hydroxyl radicals (•OH) during the photocatalytic process can also reflect the photogenerated charge separation. [41] Herein, the coumarin fluorescent method is used to detect the amount of ·OH produced. In coumarin fluorescent method, the coumarin could easily react with ·OH to produce luminescent 7-hydroxy-coumarin. As shown in Fig. 7A, B-STO-20 exhibits the strongest fluorescent response, demonstrating that charge separation is significantly improved after doping a proper amount of boron. Photoluminescence (PL) emission spectrum originating from the recombination of free charge carriers, usually serves as a good candidate for the characterization of heterostructures, indicating the process of photogenerated charge separation, migration, and transfer. [42] Fig. 7B clearly indicates that the PL intensity of STO is relatively higher, which means fast recombination of photogenerated charge carriers. However, the PL intensities of B-STO-X samples are obviously decreased after B-doping and the lowest PL signal is observed for the amount optimized B-STO-20 sample. This is in good accordance with the fluorescence results suggesting that charge separation is significantly improved.

Furthermore, photoelectrochemical experiments were performed to further prove the enhanced charge separation of B-STO-X samples. Steady-state surface photovoltage spectroscopy (SS-SPS) is an effective technique to reveal the photogenerated charge separation. From Fig. 7C, it is clear that SS-SPS response of STO is greatly enhanced after B-doping, especially for the optimal B-STO-20 sam-
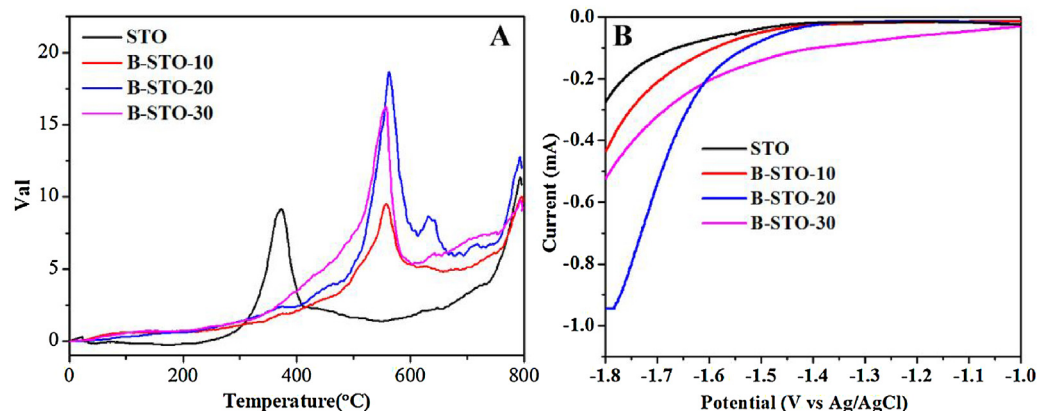
Fig. 7. Fluorescence spectra related to the produced hydroxyl radicals (A) and PL intensity peaks (B), SS-SPS responses (C) and EIS spectra (D) of STO, B-STO-10, B-STO-20 and B-STO-30 samples.

ple, suggesting that charge separation is significantly improved. This means that the B doping increases the electrostatic potential difference that boosts the internal electric field of STO. The red shift of B-doped STO samples is in good agreement with UV–vis absorption results. The EIS Nyquist plot in Fig. 7D displays a semicircle at high frequency represents the charge-transfer process, and the diameter of the semicircle reflects the charge-transfer resistance. It is clearly demonstrated that the diameters of the semicircle for B-STO-20 are much smaller than those of STO, B-STO-10 and B-STO-30, implying that a proper amount of B doping could promote the electron mobility by reducing the electron-hole pair recombination of STO and favor charge transportation and separation. This is further supported by the Mott-Schottky curves analysis as shown in Fig. S10. All the samples reveal a positive slope in the

Mott-Schottky plots, as expected for the *n*-type semiconductor, demonstrating that the B-doping doesn't change the property of STO. In addition, the carrier density (N_d) can be calculated from the slope of the Mott-Schottky plot using the following equation:[43]

$$N_d = (2/e_0 \varepsilon \varepsilon_0)[d(1/C^2)/dV]^{-1}$$

Where e_0 is the electron charge, ε is the dielectric constant, ε_0 is the permittivity of vacuum, N_d is the carrier density and V is the applied bias at the electrode. Importantly, the B-STO-20 sample shows smaller slopes of the Mott-Schottky plot compared to STO, B-STO-10 and B-STO-30, suggesting a faster charge transfer, leading to the enhanced photocatalytic CO_2 reduction efficiency. Based on the PL, •OH measurement, SS-SPS, EIS and Mott-Schottky results,

Fig. 8. CO_2-TPD (A) and electrochemical CO_2 reduction (B) of STO, B-STO-10, B-STO-20 and B-STO-30 samples.

it is concluded that the B-doping could effectively promote the charge separation of STO and suitable for efficient photocatalytic CO_2 reduction.

It is widely accepted that the surface fixation and activation of CO_2 as the consequent step of charge separation is much crucial to the photocatalytic CO_2 reduction activity. In order to investigate the CO_2 adsorption capacity of these samples, the CO_2-TPD measurements of STO, B-STO-10, B-STO-20 and B-STO-30 were performed as shown in Fig. 8. From the CO_2-TPD profile of STO, there is a strong CO_2 desorption peak with maximum at 372 °C, implying that the surface of STO could induce a certain extent of the CO_2 adsorption which may cause by the little alkalinity of strontium. As expected, the CO_2 desorption peak of B-doped STO is shifted to higher temperature region (~560 °C), indicating that the B-doping produce considerably strong CO_2 adsorption sites on the surface of STO, because of the alkaline nature of boron. The slight difference in the peak position is suspected to the different content of B. When the absorption is enhanced, CO_2 molecule is easy to fix on the surface of catalyst. The catalyzing and activation of CO_2 is the final process in photocatalytic CO_2 reduction. Moreover, the photocatalytic activity of H_2 production over different samples were also measured (Fig. S11). The results showed that the activity of photocatalytic H_2 production over STO and B-STO were poor, suggesting the surface of them is preferred to CO_2 reduction than H_2 production that further supports the high activity. In general, electrochemical reduction process, using external electric field to supply electrons, reveals the essential catalytic capacity of catalysts. The electrochemical CO_2 reduction experiments of STO, B-STO-10, B-STO-20 and B-STO-30 samples were measured as shown in Fig. 8B. It is clear that the cathodic currents of B-STO-X especially for B-STO-20 one is obviously enhanced as compared to that of STO. This gives bright evidence of the high photocatalytic CO_2 reduction activity of B-STO-20.

4. Conclusions

In summary, boron doped layered polyhedron $SrTiO_3$ nanoparticles have successfully been prepared through solid-state method using TiB_2 as boron and titanium source. The SEM, TEM and photocatalytic CO_2 reduction performance reveal that a proper content of B-doping is effective to promote the activity of STO. B-STO-20 sample is found to be the optimal one that is capable of producing 14 and 21 $\mu mol/h^{-1} g^{-1}$ of CH_4 and CO, respectively. It is clearly demonstrated that B-doping is effective to promote the charge separation and improve the surface CO_2 fixation, activation and catalysis of $SrTiO_3$ for efficient co-catalyst free photocatalytic CO_2 reduction. This work would help us to deeply understand the photophysical processes, and provide feasible routes to further improve the photocatalytic performance of nanosized oxide semiconductors for CO_2 reduction.

Acknowledgments

Appendix A. Supplementary data

Supplementary data associated with this article can be found, in the online version, at http://dx.doi.org/10.1016/j.apcatb.2017.07.024.

References

[1] L. Lin, K. Wang, K. Yang, X. Chen, X. Fu, W. Dai, Appl. Catal. B-Environ. 204 (2017) 440–455.
[2] A. Dhakshinamoorthy, S. Navalon, A. Corma, H. Garcia, Energy Environ. Sci. 5 (2012) 9217–9233.
[3] X. Zhao, B. Luo, R. Long, C. Wang, Y. Xiong, J. Mater. Chem. A 3 (2015) 4134–4138.
[4] S.N. Habisreutinger, L. Schmidt-Mende, J.K. Stolarczyk, Angew. Chem. 52 (2013) 7372–7408.
[5] Y. Ma, X. Wang, Y. Jia, X. Chen, H. Han, C. Li, Chem. Rev. 114 (2014) 9987–100043.
[6] R. Kuriki, O. Ishitani, K. Maeda, ACS Appl. Mater. Interfaces 8 (2016) 6011–6018.
[7] J. Ran, J. Zhang, J. Yu, M. Jaroniec, S.Z. Qiao, Chem. Soc. Rev. 43 (2014) 7787–7812.
[8] N. Zhang, Y. Qu, K. Pan, G. Wang, Y. Li, Nano Res. 9 (2016) 726–734.
[9] X. Guan, L. Guo, ACS Catal. 4 (2014) 3020–3026.
[10] R.P. Forslund, J.T. Mefford, W.G. Hardin, C.T. Alexander, K.P. Johnston, K.J. Stevenson, ACS Catal. 6 (2016) 5044–5051.
[11] G. Zhang, W. Jiang, S. Hua, H. Zhao, L. Zhang, Z. Sun, Nanoscale 8 (2016) 16963–16968.
[12] K. Yu, C. Zhang, Y. Chang, Y. Feng, Z. Yang, T. Yang, L.L. Lou, S. Liu, Appl. Catal. B-Environ. 200 (2017) 514–520.
[13] Y. Jia, S. Shen, D. Wang, X. Wang, J. Shi, F. Zhang, H. Han, C. Li, J. Mater. Chem. A 1 (2013) 7905–7909.
[14] J.C. Hemminger, R. Carr, G.A. Somorjai, Chem. Phys. Lett. 57 (1978) 100–104.
[15] W. Yu, J. Zhang, T. Peng, Appl. Catal. B-Environ. 181 (2016) 220–227.
[16] K. Li, B. Peng, T. Peng, ACS Catal. 6 (2016) 7485–7527.
[17] X. Zhou, J. Shi, C. Li, J. Phys. Chem. C 115 (2011) 8305–8311.
[18] S. Nazir, J. Cheng, M. Behtash, J. Luo, K. Yang, ACS Appl. Mater. Interfaces 7 (2015) 14294–14302.
[19] W. Chen, H. Liu, X. Li, S. Liu, L. Gao, L. Mao, Z. Fan, W. Shangguan, W. Fang, Y. Liu, Appl. Catal. B-Environ. 192 (2016) 145–151.
[20] B.R. Wygant, K.A. Jarvis, W.D. Chemelewski, O. Mabayoje, H. Celio, C.B. Mullins, ACS Catal. 6 (2016) 1122–1133.
[21] F. Zou, Z. Jiang, X. Qin, Y. Zhao, L. Jiang, J. Zhi, T. Xiao, P.P. Edwards, Chem. Commun. 48 (2012) 8514–8516.
[22] C. Zhang, Y. Jia, Y. Jing, Y. Yao, Int. J. Hydrogen Energy 40 (2015) 1343–1351.
[23] G. Liu, Y. Zhao, C. Sun, F. Li, G.Q. Lu, H.M. Cheng, Angew. Chem. Int. Ed. 47 (2008) 4516–4520.
[24] C. Zhang, Y. Jia, Y. Jing, Y. Yao, J. Ma, J. Sun. Com. Mater. Sci. 79 (2013) 69–74.
[25] H. Yu, J. Wang, S. Yan, T. Yu, Z. Zou, J. Photoch. Photobio. A 275 (2014) 65–71.
[26] J. Li, L. Cai, J. Shang, Y. Yu, L. Zhang, Adv. Mater. 28 (2016) 4059–4064.
[27] S. Bai, X.Y. Li, Q. Kong, R. Long, C.M. Wang, J. Jiang, Y.J. Xiong, Adv. Mater. 27 (2015) 3444–3452.
[28] X. Meng, S. Ouyang, T. Kako, P. Li, Q. Yu, T. Wang, J. Ye, Chem. Commun. 50 (2014) 11517–11519.
[29] V.P. Indrakanti, J.D. Kubicki, H.H. Schobert, Energy Environ. Sci. 2 (2009) 745–758.
[30] J. Wu, H. Cui, X. Zhang, Y. Luan, L. Jing, Phys. Chem. Chem. Phys. 17 (2015) 15837–15842.
[31] S. Martha, D.P. Das, N. Biswal, K.M. Parida, J. Mater. Chem. 22 (2012) 10695.
[32] G. Liu, L.C. Yin, J. Wang, P. Niu, C. Zhen, Y. Xie, H.M. Cheng, Energy Environ. Sci. 5 (2012) 9603–9610.
[33] J. Wang, H. Li, H. Li, S. Yin, T. Sato, Solid State Sci. 11 (2009) 182–188.
[34] K.A. Lehuta, K.R. Kittilstved, J. Mater. Chem. A 2 (2014) 6138–6145.
[35] S. In, A. Orlov, R. Berg, F. Garcia, S. Pedrosa-Jimenez, M.S. Tikhov, D.S. Wright, R.M. Lambert, J. Am. Chem. Soc. 129 (2007) 13790–13791.
[36] M. Shang, H. Hu, G. Lu, Y. Bi, J. Mater. Chem. A 4 (2016) 5849–5853.
[37] W. Zhao, W. Ma, C. Chen, J. Zhao, Z. Shuai, J. Am. Chem. Soc. 126 (2004) 4782–4783.
[38] S.C. Roy, O.K. Varghese, M. Paulose, C.A. Grimes, ACS Nano 4 (2010) 1259–1278.
[39] J. Hou, S. Cao, Y. Wu, F. Liang, Y. Sun, Z. Lin, L. Sun, Nano Energy 32 (2017) 359–366.
[40] X. Chen, S. Shen, L. Guo, S.S. Mao, Chem. Rev. 110 (2010) 6503–6507.
[41] Y. Qu, W. Zhou, Z. Ren, G. Wang, B. Jiang, H. Fu, ChemCatChem 6 (2014) 2258–2262.
[42] J. Bian, Y. Qu, R. Fazal, X. Li, N. Sun, L. Jing, J. Phys. Chem. C 120 (2016) 11831–11836.
[43] Y. Qu, W. Zhou, Y. Xie, L. Jiang, J. Wang, G. Tian, Z. Ren, C. Tian, H. Fu, Chem. Commun. 49 (2013) 8510–8512.